THE PROTEIN SOCIETY

Campylobacter jejuni adenosine triphosphate phosphoribosyltransferase is an active hexamer that is allosterically controlled by the twisting of a regulatory tail

Gerd Mittelstädt,[1,2] Gert-Jan Moggré,[1,2] Santosh Panjikar,[3,4] Ali Reza Nazmi,[5] and Emily J. Parker[1,2]*

[1]Maurice Wilkins Centre, Biomolecular Interaction Centre, Christchurch 8140, New Zealand
[2]Department of Chemistry, University of Canterbury, Christchurch 8140, New Zealand
[3]Australian Synchrotron, Clayton, Melbourne, Victoria 3168, Australia
[4]Department of Biochemistry and Molecular Biology, Monash University, Clayton, Campus, Melbourne, Victoria 3800, Australia
[5]Biomolecular Interaction Centre and School of Biological Sciences, University of Canterbury, Christchurch 8140, New Zealand

Received 11 April 2016; Accepted 11 May 2016
DOI: 10.1002/pro.2948
Published online 00 Month 2016 proteinscience.org

Abstract: Adenosine triphosphate phosphoribosyltransferase (ATP-PRT) catalyzes the first committed step of the histidine biosynthesis in plants and microorganisms. Here, we present the functional and structural characterization of the ATP-PRT from the pathogenic ε-proteobacteria *Campylobacter jejuni* (*Cje*ATP-PRT). This enzyme is a member of the long form ($HisG_L$) ATP-PRT and is allosterically inhibited by histidine, which binds to a remote regulatory domain, and competitively inhibited by AMP. In the crystalline form, *Cje*ATP-PRT was found to adopt two distinctly different hexameric conformations, with an open homohexameric structure observed in the presence of substrate ATP, and a more compact closed form present when inhibitor histidine is bound. *Cje*ATP-PRT was observed to adopt only a hexameric quaternary structure in solution, contradicting previous hypotheses favoring an allosteric mechanism driven by an oligomer equilibrium.

Abbreviations: ATP-PRT, adenosine triphosphate phosphoribosyltransferase; BTP, 1,3-bis[tris(hydroxymethyl)methylamino]propane; *Cje*ATP-PRT, ATP-PRT from *Campylobacter jejuni*; *Eco*ATP-PRT, *Escherichia coli* ATP-PRT; His, l-histidine; ITC, isothermal titration calorimetry; *Mtu*ATP-PRT, *Mycobacterium tuberculosis* ATP-PRT; PDB, Protein Data Bank; PR-ATP, phosphoribosyl ATP; PRPP, phosphoribosyl pyrophosphate; PRT, phosphoribosyltransferase; RMSD, root-mean-square difference; *Sen*ATP-PRT, *Salmonella enterica* subsp. *enterica* Typhimurium ATP-PRT

Additional Supporting Information may be found in the online version of this article.

Significance Statement: ATP-phosphoribosyltransferase catalyzes the first dedicated step in the biosynthesis of the essential amino acid histidine in microorganisms. We report the functional characterization of this enzyme from human pathogen *Campylobacter jejuni*. The enzyme is inhibited by histidine, allowing for tuned production of histidine in response to cellular demands. Our results reveal how the enzyme structure becomes compressed when histidine binds and exposes the molecular details of how this enzyme performs its function.

Grant sponsors: Maurice Wilkins Centre and by New Zealand Lottery Health; Grant sponsor: University of Canterbury Doctoral Scholarships (G.M. and G-J.M.).

*Correspondence to: Emily J. Parker, Department of Chemistry, University of Canterbury, Private Bag 4800, Christchurch 8140, New Zealand. E-mail: emily.parker@canterbury.ac.nz

Instead, this study supports the conclusion that the ATP-PRT long form hexamer is the active species; the tightening of this structure in response to remote histidine binding results in an inhibited enzyme.

Keywords: ATP-PRT; phosphoribosyltransferase; HisG; allostery; conformational change

Introduction

Histidine biosynthesis, the primary metabolic pathway responsible for the *de novo* synthesis of the proteogenic amino acid L-histidine (His), is energetically expensive, requiring 41 equivalents of ATP to synthesize a single His molecule.[1] The pathway involves a total of 10 reactions and also contributes metabolites to the *de novo* purine synthesis via its branch point at the imidazole-glycerol phosphate synthase reaction, which helps the cell to replenish its energy pool (Fig. 1). Adenosine triphosphate phosphoribosyltransferase (ATP-PRT) catalyzes the first committed step of His biosynthesis and represents the major control point for its regulation via feedback inhibition by the pathway end-product His.

The phosphoribosyltransferase (PRT) enzyme family, to which ATP-PRT belongs, is characterized by the ability to catalyze the displacement of pyrophosphate from substrate phosphoribosyl pyrophosphate (PRPP) by a nitrogen-containing nucleophile. PRT enzymes are found predominantly in the nucleotide metabolism, but also in amino acid biosynthesis, and are divided into four types according to their overall fold and domain architecture. ATP-PRT represents its own unique type, denoted type IV PRT.[2] ATP-PRT enzymes can be further subdivided into two groups based on their sequence length and their distinctly different quaternary structures. The long form of ATP-PRT (known as $HisG_L$) has a chain length of 280–310 amino acids and assembles only as a homomeric form. The short form ($HisG_S$) consists of only 200–220 amino acid residues per chain and associates with a second gene product, the tRNA synthetase paralog HisZ,[3] to form a fully functional complex.[4] While both forms carry out the same biochemical role and show clear structural similarity in their catalytic domains, most organisms encode for only one type of ATP-PRT, except the *Geobacter* clade,[5] suggesting an early evolutionary division.[6]

The ATP-PRT-catalyzed reaction is the reversible substitution of PRPP by ATP, releasing pyrophosphate. The product phosphoribosyl ATP (PR-ATP) is then converted irreversibly by the subsequent enzymes of the pathway, driving the reaction in the biosynthetic direction. Mg^{2+} ions are required for the activation and stabilization of the polyphosphorylated substrates and are thus essential for the reaction to occur.[7] Extensive kinetic characterization was carried out on the ATP-PRT enzyme ($HisG_L$) from *Salmonella enterica* subsp. *enterica* Typhimurium (*Sen*ATP-PRT)[7–9] according to which the reaction follows an ordered sequential mechanism with ATP binding the enzyme first and PR-ATP leaving last. ATP-PRT has been reported to be inhibited by a variety of compounds. Due to the equilibrium nature of the reaction, substrates and products naturally compete for the active site, but the most potent inhibition is achieved by a combination of the nucleotide AMP and the pathway end-product His, which act synergistically.[10] Individually AMP, and to a lesser extent also ADP, inhibit ATP-PRT competitively with respect to both substrates. This is strongly supported by the observation that AMP binds the active site of *Escherichia coli* ATP-PRT (*Eco* ATP-PRT).[11] ATP-PRT activity and consequently the metabolite flux into His biosynthesis, is therefore determined by the energy state of the cell as reflected by the ATP to AMP ratio.[1,12] His on the other hand acts as an allosteric inhibitor, exhibiting

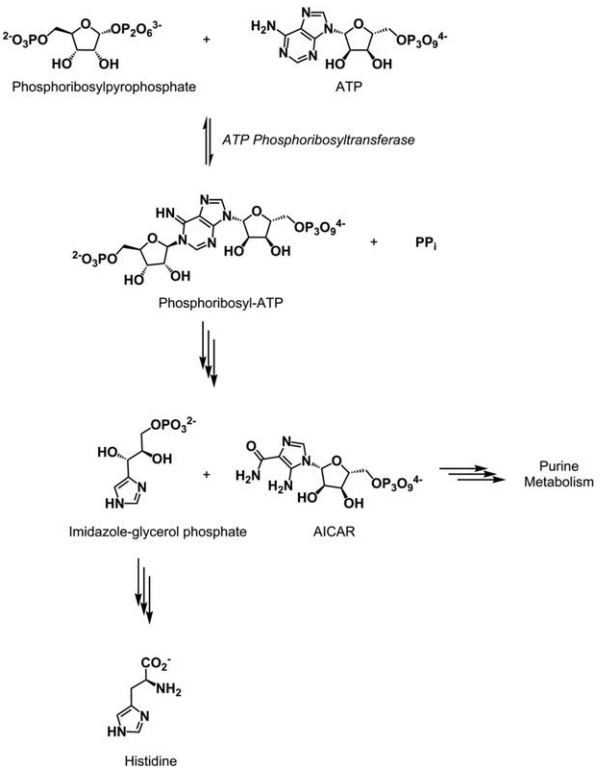

Figure 1. Histidine biosynthesis. ATP-PRT catalyzes the first committed step of the *de novo* synthesis of His. The formation of the His precursor imidazole-glycerol phosphate leads to the side product 5-aminoimidazole-4-carboxamide ribonucleotide (AICAR), which is used in the purine metabolism.

Table I. *Steady-State Kinetic Parameters for ATP-PRT*

Parameter	*Cje*ATP-PRT[a]	*Sen*ATP-PRT[8]	*Mtu*ATP-PRT[14]
$K_{M\ ATP}$ (μM)	97 ± 10	110	263 ± 63
$K_{M\ PRPP}$ (μM)	15 ± 1	15	49 ± 6
k_{cat} (s^{-1})	1.8 ± 0.1	–	0.31 ± 0.01
$k_{cat}/K_{M\ ATP}$ (s^{-1} mM^{-1})	19 ± 2		1.2 ± 0.3
$k_{cat}/K_{M\ PRPP}$ (s^{-1} mM^{-1})	120 ± 10		6.3 ± 0.8
$K_{i\ AMP}$ (ATP) (μM)	356 ± 22	480	
$K_{i\ AMP}$ (PRPP) (μM)	382 ± 34	550	
$K_{i\ His}$ (ATP) (μM)	44 ± 7	–	27.9 ± 1.9
$K_{i\ His}$ (PRPP) (μM)	40 ± 1	–	25.7 ± 12.8

[a] Generated by global fitting, using *Cje*ATP-PRT (280 nM), and *Eco*PPase (6.4 μM) in 50 m*M* Tris/HCl, $MgCl_2$ (10 m*M*), NaCl (100 m*M*), KCl (50 m*M*), pH 8.5 at 25°C. (-) k_{cat} and K_I data for *Sen* ATP-PRT has not been reported.

non-competitive and uncompetitive inhibition patterns against the substrates in *Sen*ATP-PRT[13] and *Mycobacterium tuberculosis* ATP-PRT (*Mtu*ATP-PRT).[14] In $HisG_L$ His binding occurs in a remote regulatory binding site in a discrete domain and the binding has been observed for both *E. coli* and *M. tuberculosis* enzymes.

Crystal structures have been determined for both long form and short form ATP-PRT enzymes. The long form ATP-PRT, represented by the *E. coli*[11] and *M. tuberculosis*[15] enzymes, possesses a homohexameric structure with a 2- and 3-fold internal symmetry, where all active sites are secluded in the interior of the protein. Each chain consists of three distinct domains. Domains I and II both have mixed α-β open twisted sheet folds, with the active site located in the cleft between them. This bilobal "catalytic core" forms the basis of ATP-PRT function and is the common structural characteristic between short and long form enzymes.[16] The C-terminal domain III is exclusive to the ATP-PRT long form and arranges in two trimeric units, one on either end of the hexamer. This domain has been identified to be an ACT domain (named from aspartokinase, chorismate mutase and TyrA)[17,18] responsible for the feedback regulation. Three His binding sites have been observed in both trimeric regulatory regions of the protein in the *Mtu*ATP-PRT (PDB ID: **1NH8**) and archaeal *Methanothermobacter thermautotrophicus* ATP-PRT (PDB ID: **2VD3**) structures. A number of key residues for His binding have also been identified in *Corynebacterium glutamicum* ATP-PRT, which lowered the sensitivity of the enzyme towards His upon mutation[19] confirming the identified binding site as the functional allosteric site. The remarkably different structure of the heterooctameric $HisG_S$/Z complex is made up of four HisZ chains in a central X-shaped unit and two $HisG_S$ dimers on opposite sides. His binding to this complex has been observed at several places in the interface between the HisG and HisZ chains.[4,20]

Based on the involvement of the ACT domains in His binding at the interfaces between the chains of the homohexameric form, it was proposed that the hexamer represents the inhibited form of the enzyme, whereas the active species, without His bound, was thought to be dimeric.[2,15] This is consistent with earlier analysis of the oligomeric state of *Eco*ATP-PRT, where multiple species have been detected.[21,22] However, more recent results fail to support the existence of a stable dimeric form of the *Mtu*ATP-PRT enzyme, making an oligomeric equilibrium unlikely.

In this study, we examine the biochemical and regulatory properties of the $HisG_L$ ATP-PRT from *Campylobacter jejuni* (*Cje*ATP-PRT). Through structures showing the binding of ligands at both the active and allosteric sites and complementary solution state observations, we illuminate an allosteric mechanism that involves conformational change of an open homohexameric active protein to a closed hexameric His-bound inhibited form.

Results

C. Jejuni ATP-PRT is inhibited by AMP and His, and more potently by an AMP/His-combination

Highly purified *Cje*ATP-PRT enzyme was found to be active under the described assay conditions and the kinetic parameters were determined (Table I). Reaction kinetics followed a sequential mechanism and optimal concentrations for Mg^{2+} and Na^+/K^+ were found to be 10 m*M* and 100–200 m*M*, respectively (Supporting Information Figs. S2 and S3). The derived kinetic parameters also show good agreement with those of long form ATP-PRTs from other sources.[8,10,14]

*Cje*ATP-PRT activity was shown to be susceptible to inhibition by the native inhibitors AMP and His. Moreover, the two inhibitors show a clear synergistic behavior towards the inhibition of *Cje*ATP-PRT, a known phenomenon of the long form ATP-PRT.[10] The effect was most prominent for inhibitor mixtures at concentrations that only marginally reduce the enzyme activity (5–20% activity loss) individually (Fig. 2).

While our results depict standard competitive inhibition for the effect of AMP with respect to both ATP and PRPP, for *Cje*ATP-PRT the allosteric inhibitor His was found to follow a non-competitive model

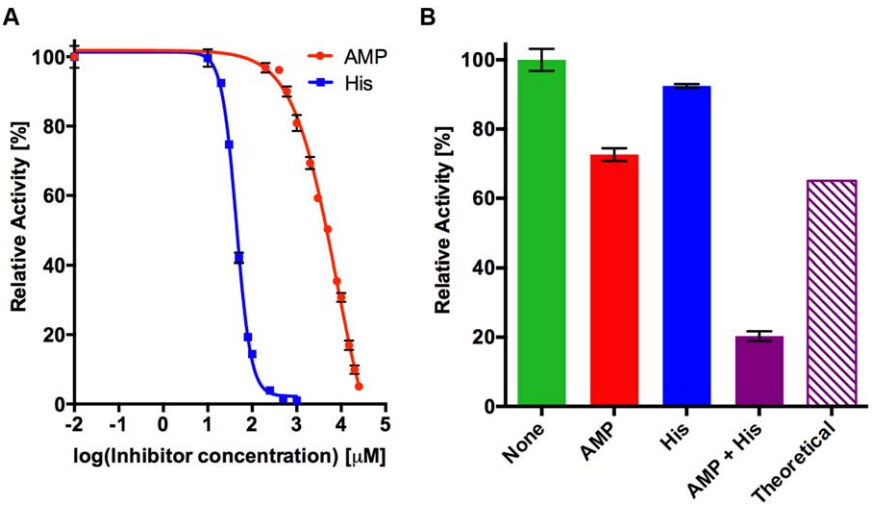

Figure 2. Inhibition of *C. jejuni* ATP-PRT. Relative activity of *Cje*ATP-PRT in the presence of the inhibitors AMP and His. Error bars represent standard deviations of the measurements at each point. A: Dose response curves and IC_{50} fits for His and AMP individually. B: The synergistic effect of both inhibitors shown as columns. The activity was determined in the presence of no inhibitor (none), 2 m*M* AMP (AMP), 20 μ*M* His (His), and both 2 m*M* AMP and 20 μ*M* His (AMP + His). For comparison, a theoretical value is given representing the simple addition of the individual AMP and His inhibitory effects.

of inhibition with respect to both substrates (Supporting Information Fig. S4). The resulting inhibition constants for AMP and His are consistent with kinetically obtained values for *Sen*ATP-PRT (AMP)[10] and *Mtu*ATP-PRT (His)[14] (Table I).

Complex binding of His and AMP

The strong binding of His to *Cje*ATP-PRT, seen in the kinetic assay, was confirmed by ITC experiments, which also show a clear cooperativity between multiple binding events for the enzyme (fitted with a sequential binding model). When His alone was titrated against the *Cje*ATP-PRT a strong initial exothermic signal was seen that quickly declined in subsequent injections. Thereafter the curve has a bi-phasic shape. The binding constants (K_d) for His range between 15 and 50 μ*M*.

A very differently shaped isotherm was observed when His was titrated into the enzyme in the presence of 1 m*M* AMP. In this case the binding followed a sequential model with two binding events, giving rise to K_d values that are lower than observed for His alone, indicating a higher affinity of the enzyme for His in the presence of AMP. Likewise, the binding constant of AMP for the enzyme was also shown to decrease approximately 6-fold in the presence of 1 m*M* His (Table II).

In contrast to His, the binding of the active site inhibitor AMP follows the classic single-site model, highlighting that all present active sites are equivalent. The resulting K_d value is significantly lower than the kinetically measured $K_{i\ AMP}$ values, which is consistent with the competitive nature of AMP towards both substrates and the kinetic determination of K_i in the presence of saturating concentrations of either substrate. Consequently, AMP-titration in the presence of 1 m*M* ATP resulted in a higher K_d value (83 ± 8 μ*M*).

Table II. *Isothermal Titration Calorimetry*

Ligand	Parameter			
	K_d (μ*M*)	Stoichiometry	Δ*H* (kcal/mol)	Δ*S* (cal/mol)
ATP[a]	158 ± 13	1.07 ± 0.08	−2.5 ± 0.2	9.1
AMP[b]	51 ± 4	1.00 ± 0.04	−11.3 ± 0.6	−18.4
AMP[c]	8.3 ± 0.2	1.14 ± 0.01	−11.5 ± 0.1	−15.2
His[d]	19.3 ± 0.2, 14.5 ± 0.2, 36 ± 1, 50 ± 1, 47 ± 1	ND[e]	−14.9 ± 0.2	−32.0
His[f]	4.8 ± 0.7, 2.3 ± 0.1	0.91 ± 0.20	−24.2 ± 1.0	−57.1

Parameters derived from the ATP, AMP and His titrations against 100 μ*M* *Cje*ATP-PRT. Errors are derived from data fits.
[a] 4 m*M*, single site model.
[b] 3.5 m*M*, single site model.
[c] 2 m*M*, in the presence of 1 m*M* His, single site model.
[d] 1.5 m*M*, sequential binding model (five events).
[e] Not determined (ND) due to the complex binding
[f] 1 m*M*, in the presence of 1 m*M* AMP, sequential binding model (two events).

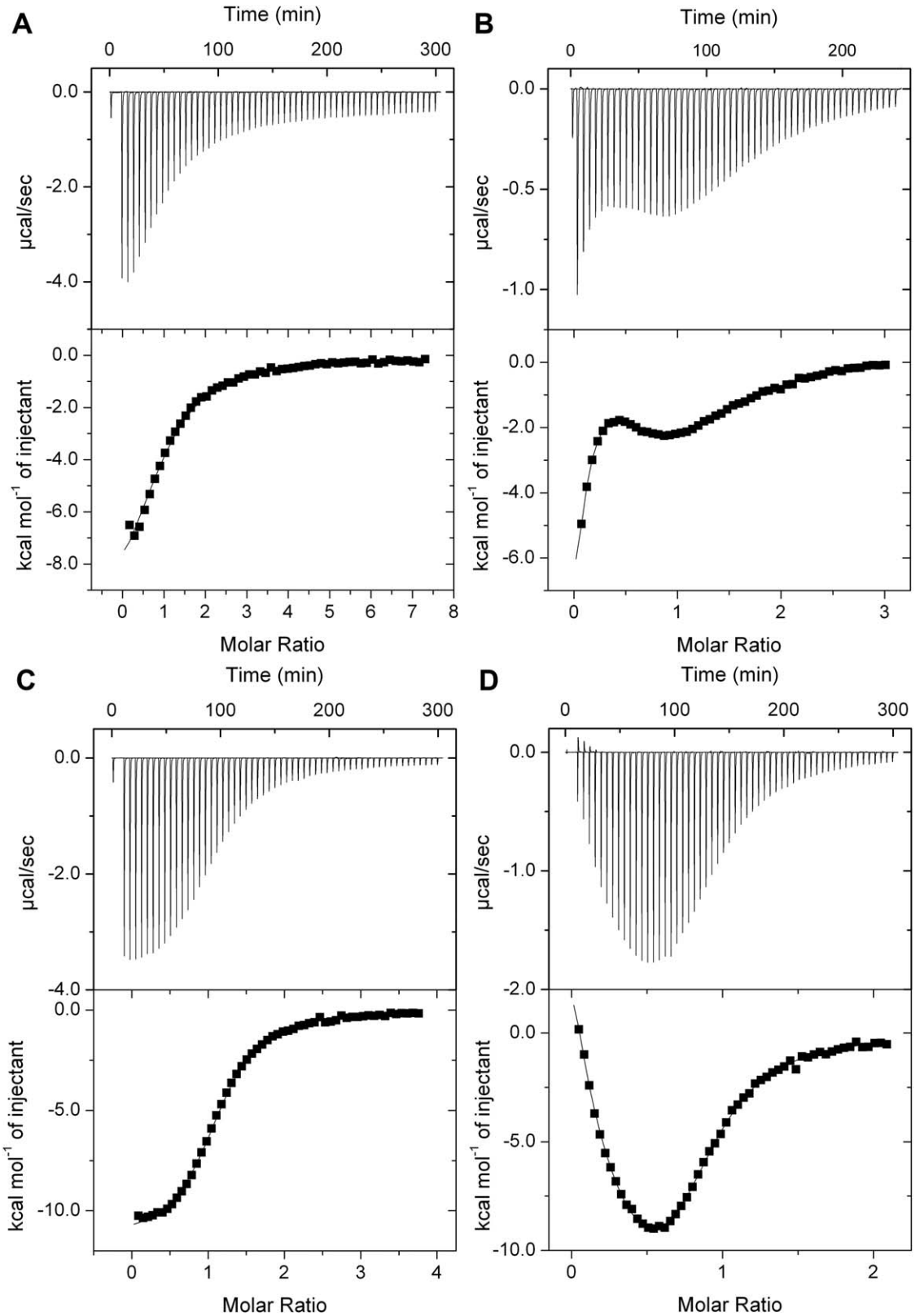

Figure 3. Inhibitor binding to *Cje*ATP-PRT. ITC isotherms resulting from the titration against *Cje*ATP-PRT, subtracted by the corresponding heat of dilution data series, and fitted using OriginLab® version 7.0 (OriginLab Corp.) A: 3.5 m*M* AMP, B: 1.5 m*M* His, C: 2 m*M* AMP in the presence of 1 m*M* His, D: 1 m*M* His in the presence of 1 m*M* AMP.

Additionally, the presence of His was shown to have a dramatic influence on the ATP binding ability of *Cje*ATP-PRT. In the absence of other ligands, ATP can readily bind to the enzyme, resulting in a K_d value close to the kinetically determined K_M value of 97 ± 10 μM. In contrast, the presence of

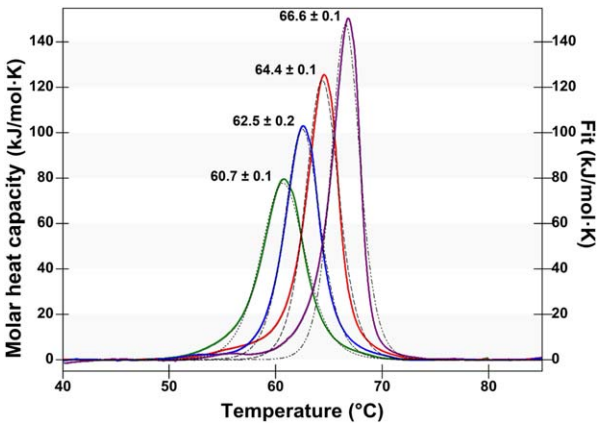

Figure 4. Effect of ligand binding on thermostability. DSC scans of *Cje*ATP-PRT were determined in 50 m*M* Tris/HCl, 100 m*M* NaCl, 5 m*M* $MgCl_2$, pH 8.5 in the presence of no ligand (green), 1 m*M* His (blue), 2 m*M* AMP (red), and the mixture of the latter two (purple). Dotted lines correspond to the fit. Midpoint temperatures of the thermal unfolding are given next to the peaks.

1 m*M* His led to no measurable ATP binding signal (Supporting Information Fig. S5).

The binding of AMP and His also affects the stability of *Cje*ATP-PRT, visible as shifts of the thermal denaturation temperature determined by DSF and DSC experiments (Supporting Information Table S6). The addition of 1 m*M* His and 2 m*M* AMP increased the melting temperature by 2 and 3°C, respectively. This stabilization effect appeared to be additive with a shift of 5° when a combination of AMP and His as added (Fig. 4).

CjeATP-PRT is hexameric

The quaternary structure of highly pure *Cje*ATP-PRT in solution was explored using AUC, as well as analytical SEC and SEC-coupled static light scattering techniques. A set of three low protein concentrations (3.0, 1.5, and 0.74 μ*M*) was used for sedimentation velocity experiments. The resulting normalized size distribution functions (Fig. 5) show one major species with a sedimentation coefficient of 7.9 S in all three preparations. The derived molecular weight of 184 kDa is close to the theoretical mass corresponding to a hexamer, 202 kDa. The existence of a single hexameric species in solution was also confirmed by the results of SEC (204 kDa) and SEC-coupled static light scattering (188 kDa) (Supporting Information Fig. S7). As the lowest measured enzyme concentrations is very close to the kinetic assays concentration of 0.28–0.44 μ*M*, it is apparent that *Cje*ATP-PRT mainly exists as a hexamer under assay conditions.

CjeATP-PRT crystallizes as a homohexamer in the presence of ATP, AMP, and His

Datasets were collected from three different *Cje*ATP-PRT co-crystals featuring the ligands ATP, AMP and His, and His alone (Table III). ATP-bound *Cje*ATP-PRT (PDB code: **4YB7**) was solved in space group *P*1 and the unit cell contains 12 chains forming two complete hexamers (0.50 Å RMSD between hexamers). A single Mg^{2+}-bound ATP molecule is found in the active site of each chain. The two inhibitor-bound structures were solved in space group $P2_1$ and contain six chains each in an asymmetric unit, arranged in a single hexamer. Both His-bound (PDB code: **4YB5**) and AMP and His-bound (PDB code: **4YB6**) structures feature six well-defined His molecules bound to the regulatory sites of the hexamer. The latter additionally contains one AMP molecule per active site. Mg^{2+} ions were observed in the active sites containing both ATP and AMP. Depending on the individual chains, a small number of residues (4–11) are disordered and not visible in the electron density map. The areas of missing residues include the N-terminus, as well as external loops (α1-β2, β6-α4, and β13-β14 loops).

Each individual *Cje*ATP-PRT chain is composed of 10 α-helices, 16 β-strands and the connecting loops. Every chain is arranged in three domains, domains I, II, and III, adopting the same overall architecture as both *Mtu*ATP-PRT and *Eco*ATP-PRT.[11,15] *Cje*ATP-PRT domain I is composed of residues 1–103 and 191–225, which form a Rossmann fold, commonly found for nucleotide binding proteins.[23] Residues 104–190 form domain II, which is inserted into domain I between the two β-strands β5 and β11. Together the two domains form a bilobal core unit that contains the catalytic site in the cleft between them, where the binding of ATP and AMP is observed. The last 74 C-terminal residues form domain III, a regulatory ACT domain.[18] The

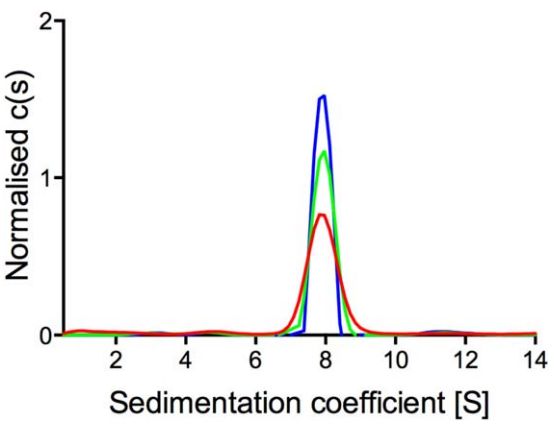

Figure 5. AUC analysis of *Cje*ATP-PRT. Sedimentation velocity experiments were performed in 10 m*M* Tris/HCl, 100 m*M* NaCl, 5 m*M* $MgCl_2$, pH 8.5 using 0.1 mg/mL (blue), 0.05 mg/mL (green), and 0.025 mg/mL (red) *Cje*ATP-PRT. Continuous size distribution functions were generated using SEDFIT,[21] normalized by the total area under the curve and smoothed with a four point moving average using Prism 6.0 (GraphPad Software).

Table III. *Crystal Parameters, Data collection, and Refinement Statistics*

	*Cje*ATP-PRT		
	ATP	His	His/AMP
A. *Data collection*			
Crystal system, space group	Triclinic, *P*1	Monoclinic, *P*2	Monoclinic, $P2_1$
Unit cell parameters			
a, *b*, *c* (Å)	91.67, 91.83, 154.90	91.14, 123.22, 95.70	91.87, 124.91, 92.81
α, β, γ (°)	101.11, 95.21, 118.14	90.00, 110.66, 90.00	90.00, 115.86, 90.00
Resolution range (Å)	50.00–2.20 (2.24–2.20)	50.00–2.24 (2.28–2.24)	50.00–1.98 (2.01–1.98)
Total reflections	839,825	472,477	493,057
Unique reflections	212,958	94,235	127,994
Redundancy	3.9 (4.0)	5.0 (4.5)	3.9 (3.9)
Completeness (%)	98.1 (97.3)	89.9 (89.7)	98.1 (96.9)
$<I/\sigma(I)>$	9.8 (1.8)	9.9 (2.4)	14.6 (2.9)
R_{merge}	0.076 (0.841)	0.093 (0.795)	0.059 (0.422)
R_{meas}	0.108 (1.189)	0.119 (1.027)	0.081 (0.584)
$CC_{1/2}$	0.982 (0.568)	0.997 (0.625)	0.998 (0.837)
Wilson *B*-value (Å^2)	36.8	43.8	21.3
Matthews coefficient (Å/Da)	2.72	2.48	2.37
B. *Refinement*			
Resolution (Å)	48.04–2.20	48.04–2.24	48.04–1.98
R_{cryst}	0.236	0.211	0.203
R_{free}	0.259	0.241	0.220
Chain length	300	300	300
Observed number of residues	2x292, 2x293, 3x294, 1x295, 4x296	2x290, 1x291, 1x292, 2x295	1x289, 1x290, 1x293, 2x295, 1x296
Water molecules	365	128	714
Other	12 ATP, 12 Mg^{2+}, 6 PO_4^{3-}, 1 acetate	6 His, 8 SCN^-, 5 K^+, 3 PEG	6 His, 6 AMP, 9 Mg^{2+}, 6 PEG
Mean *B* (Å^2)			
Protein	47.13	50.03	24.58
Water	35.20	38.62	26.94
Other ligand	55.83	61.30	45.09
	51.27	34.64	13.06, 24.81
RMSD from target values			
Bond lengths (Å)	0.009	0.012	0.009
Bond angles (°)	1.470	1.465	1.372
Dihedral angles (°)	0.073	0.075	0.077
Ramachandran			
Preferred (%)	98.22	98.56	98.36
Allowed (%)	1.78	1.44	1.64
Outliers (%)	0.00	0.00	0.00
PDB entry	4YB7	4YB5	4YB6

allosteric inhibitor His is bound at the interface of two of these domains (Fig. 6).

In all three structures, the *Cje*ATP-PRT chains assemble into homohexamers via interaction at two main interfaces. The first of these, the "dimer interface", is created between the catalytic domains of two adjacent chains and buries an area of 950–1000 Å^2 (**4YB6** and **4YB7**), and 1150–1200 Å^2 (**4YB5**), corresponding to 6–8% of the overall surface of a single chain. The second interface, the "trimer interface," contributes significantly to the overall hexameric structure. This interface predominantly involves interactions of domain III: Domain III from three neighboring chains each come together to form two trimeric arrangements at either end of the formed hexamer, placing all active sites on the inside of the hollow-centred complex. Accordingly, the trimer interface occurs six times per hexamer and is generated between the two different faces of neighboring domain IIIs, so that each domain contributes to two interfaces. The main point of interaction is the C-terminal β-strand β16 (residues K296-L298), which is donated into the β-sheet of the adjacent chain's ACT domain. According to the analysis of the structure with PDBe PISA,[24] the trimer interface was classified as essential for the *Cje*ATP-PRT hexamer, with a higher complex formation significance score (0.54–0.62) than the dimer interface (0.33–0.38) in all three *Cje*ATP-PRT structures, which is consistent with the solution oligomeric state analysis results. This directly contrasts with the previous analysis of the *Mtu*ATP-PRT and *Eco*ATP-PRT interfaces,[11] which deemed the dimer interface the more significant of the two (Supporting Information Table S9).

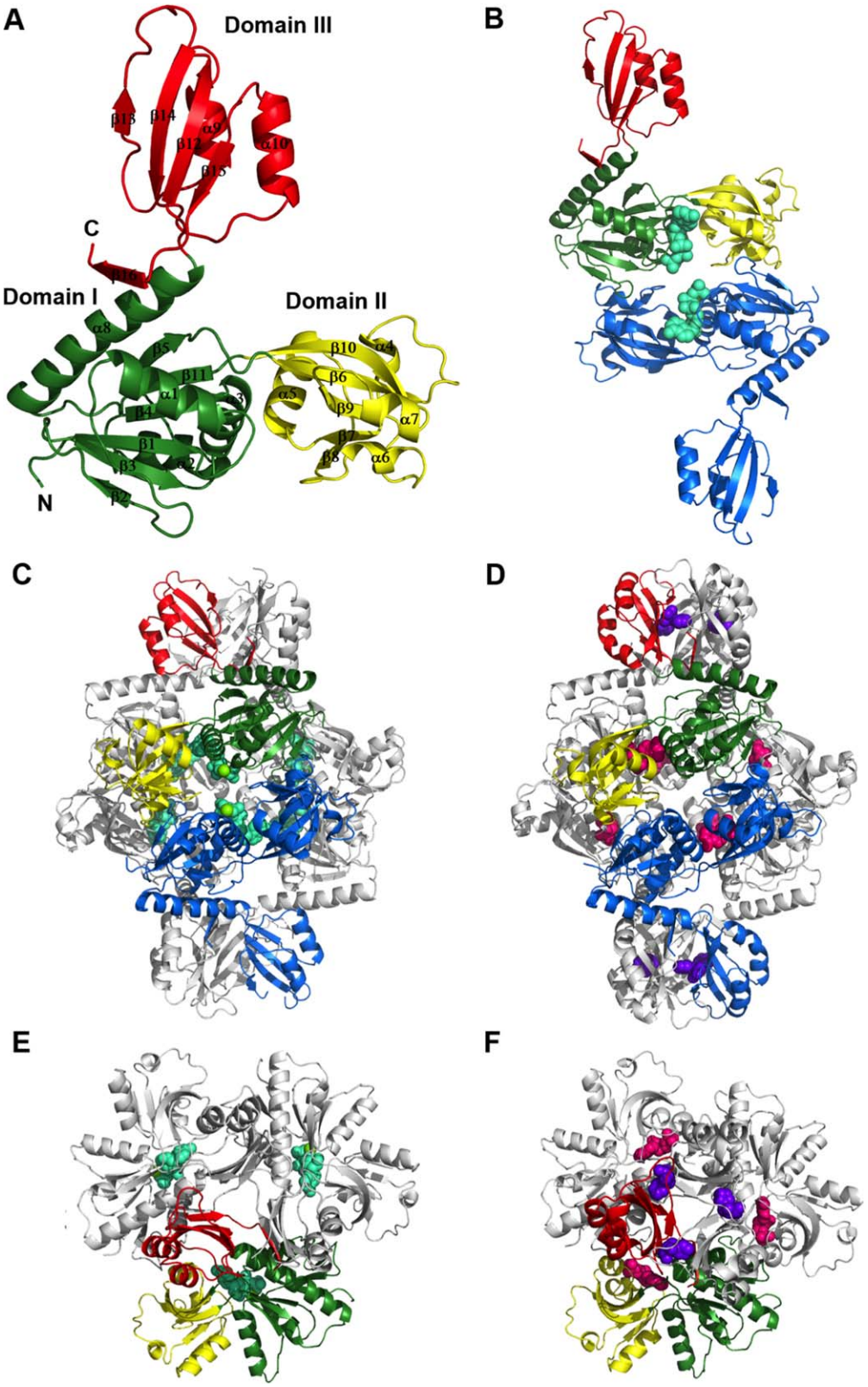

Figure 6. The *Cje*ATP-PRT structure. Architecture of the *Cje*ATP-PRTstructure as cartoon representation. A: Single chain of the ATP-bound *Cje*ATP-PRT. Domains I (green), II (yellow), and III (red) are highlighted separately. Secondary structure elements are labeled according to the sequence. B: View on two chains with bound ATP in their dimeric arrangement, facing the dual active site cavity in the center of their interface. Second chain highlighted in blue. C-F: The hexameric complex of *Cje*ATP-PRT with bound ATP (C + E) and bound His and AMP (D + F) shown from two different angles with two single chains colored according to B. The ligands ATP (cyan), His (purple), and AMP (pink) are displayed as spheres.

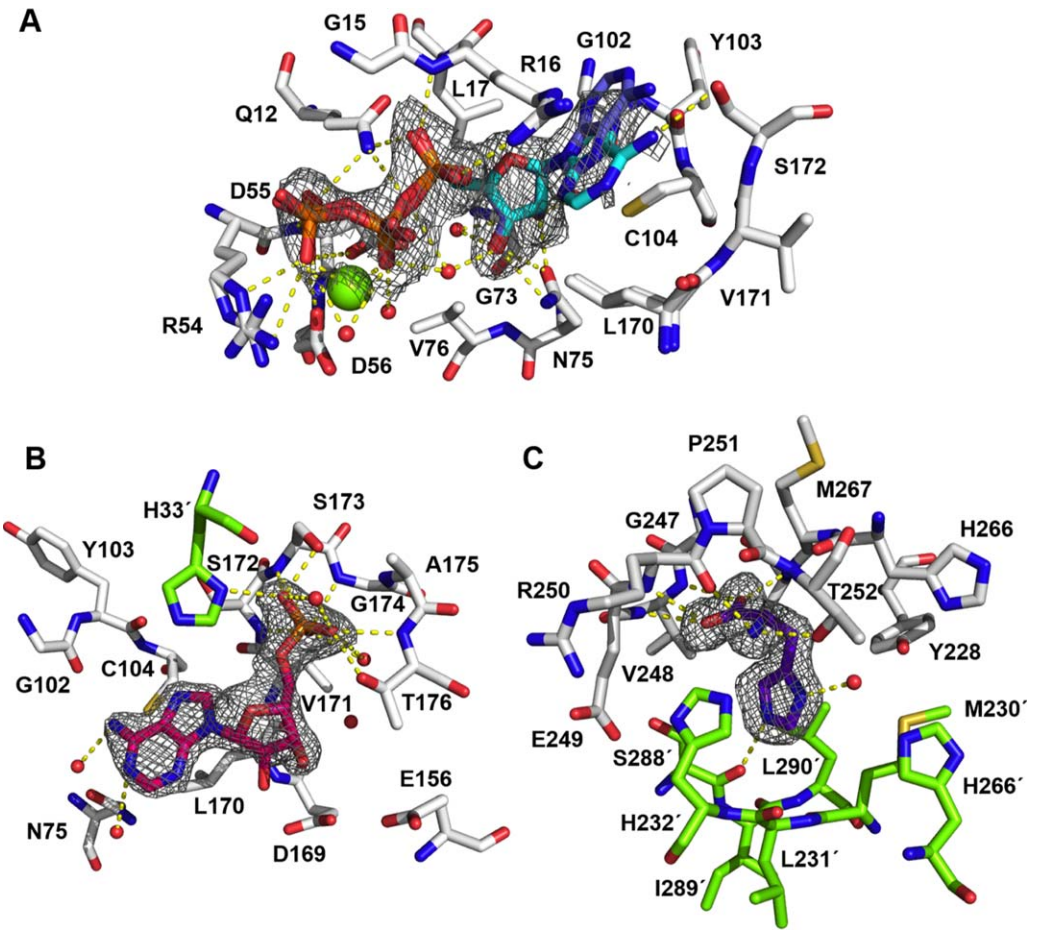

Figure 7. *Cje*ATP-PRT ligand binding. Real space representation of ATP (A), AMP (B), and His (C) surrounded by the observed electron density (Fo-Fc map, contoured at 2.0 sigma, gray mesh) and the *Cje*ATP-PRT residues of the corresponding (white) and adjacent chain (green) as sticks. Water molecules (red) and the Mg^{2+} ion (green) are represented as spheres. Heteroatoms are colored according to element: oxygen (red), nitrogen (blue), phosphorous (orange).

ATP binding is consistent with a sequential mechanism

In the ATP-bound *Cje*ATP-PRT structure all chains crystallized in the same conformation, previously described as the "active" conformation.[15] The representation of an active enzyme complex by this structure is underlined by its ability to bind substrate ATP. In the observed binding mode ATP occupies the majority of the active site, but does not involve the conserved 14 amino acid PRT signature motif,[25] a fold characteristic to type I and IV PRT enzymes, including the PRPP loop that is known to specifically bind phosphate-groups or chemically similar compounds and plays a key role in PRPP recognition. This finding is in line with a sequential binding mechanism, in which ATP can bind first, leaving the active site open for interaction with PRPP.

To our best knowledge this is the first study of an ATP-PRT structure describing convincing electron density for ATP with full occupancy. Here, ATP is accommodated in the nucleotide binding groove of domain I, involving interaction with a number of residues that are in part conserved (Supporting Information Fig. S8). The triphosphate moiety of ATP is flanked by the side chains of Arg54 and Arg16, which form hydrogen bonds to the γ and α-phosphate, respectively. A distinguishing feature of the ATP binding site is the presence of a Mg^{2+} ion in complex with the bound ATP triphosphate. This ion is coordinated in an octahedral arrangement created by the side chains of residues D55 and D56, the β and γ-phosphate of ATP, and two water molecules. This coordination embeds the Mg^{2+} into the binding site of *Cje*ATP-PRT and provides strong interaction with the substrate. The ATP ribose ring is positioned in a cavity created by the backbone and short side chains of Leu17, Gly73, Gly102, Ser191, Arg192 and Ala193 and the ribose oxygen atoms form hydrogen bonding interactions with the functionally conserved residue Asn75. The adenine portion of ATP is held in place by hydrophobic interactions with the side chain of Arg16 on one side and Leu170 and Cys104 on the other side. This "hydrophobic stack" allows the adenine to adopt two different orientations. Adenine was observed in either a catalytic relevant position, placing the N_1 nitrogen close to the expected

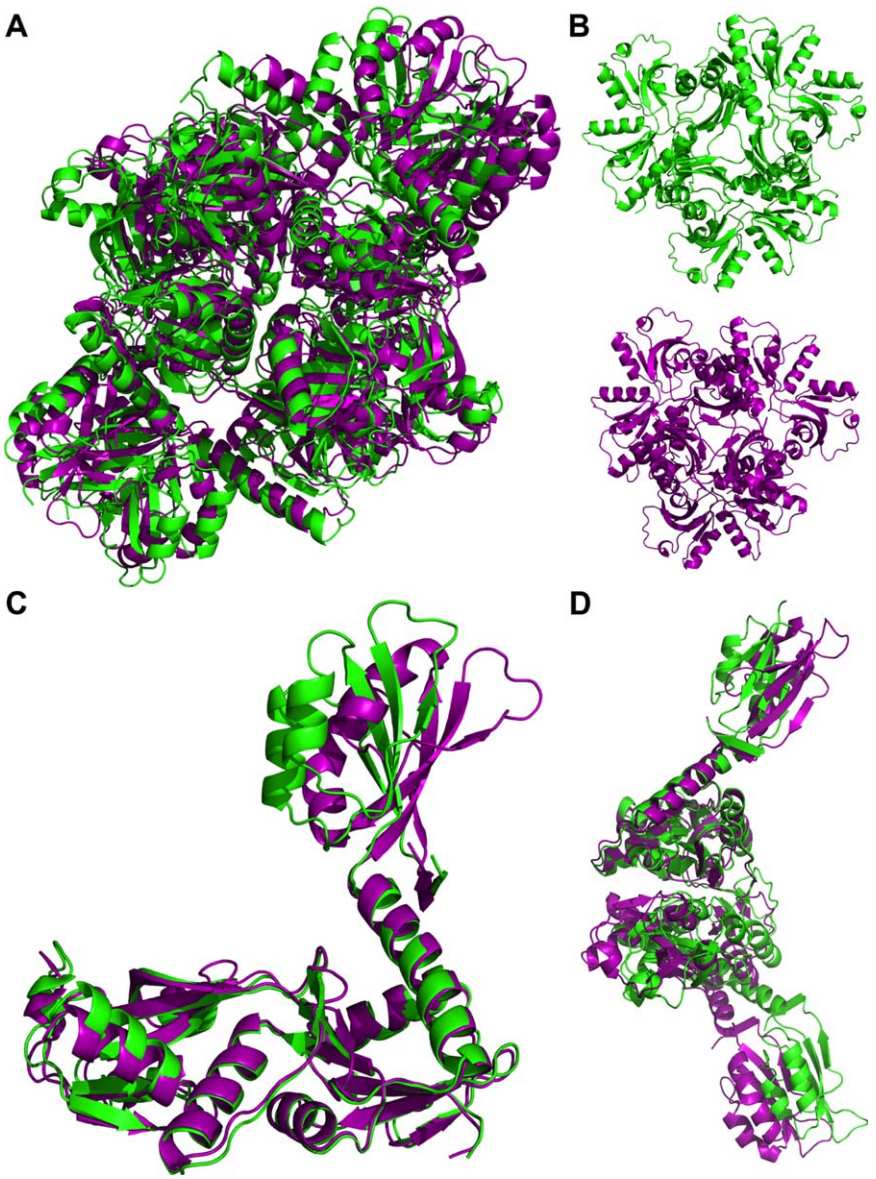

Figure 8. Changes induced by His binding. A series of superimpositions of the ATP-bound (green) and His-bound (purple) conformations of *Cje*ATP-PRT shown as cartoon representations. A: Complete hexamers. B: Trimeric units side by side. C: Single chains superimposed on the catalytic core domains. D: Dimeric unit superimposed on the catalytic core of the upper chain.

PRPP binding site, or flipped by an 180° rotation, moving N_1 away from the possible reaction site [Fig. 7(A)]. The ATP conformers were populated throughout the 12 chains, nine showing the catalytically relevant orientation and three the non-relevant, without a distinguishable pattern.

AMP binding mode confirms competitive behavior towards ATP

Overall the AMP binding mode found in *Cje*ATP-PRT confirms the results of the AMP-bound *Eco*ATP-PRT structure,[11] with the main point of interaction being the PRPP binding loop [Fig. 7(B)]. Residues Ser172-Thr176 tightly coordinate the phosphate group of AMP by hydrogen bonding interactions with their backbone nitrogen atoms and the side chain oxygen atoms of Ser173 and Thr176. On the other end of the AMP molecule, the adenine is found stacked with Leu170, as described for ATP, but with an inverted orientation. Consequently, AMP and ATP binding modes overlap in this region of the active site, which strongly supports the competitive characteristic of AMP towards both substrates observed in the kinetic analysis (Supporting Information Fig. S10).

Differences between the His-bound and AMP- and His-bound structures are minimal. The catalytic subunits of the His-bound and AMP and His-bound *Cje*ATP-PRT are very similar (RMSD = 0.34 ± 0.2 Å) with the position of the α7 helix being the only significant difference. This helix is shifted inwards by approximately 4 Å in respect to the hexamer surface in the AMP and His-bound structure, which is likely

due to the presence of AMP restricting the conformational freedom of the surrounding PRPP binding loop.

CjeATP-PRT exists in two distinct conformational states

As described for *Mtu*ATP-PRT previously,[15] the presented crystal structures of *Cje*ATP-PRT represent two distinctly different conformations. The ATP-bound structure (**4YB7**) differs decisively from the His-bound structures (**4YB5** and **4YB6**) by its overall hexamer conformation, which is apparent by the differences in the orientation of the individual chains towards each other and the consequent changes in their interfaces (Figs. 6 and 8). In comparison to the ATP-bound hexamer (117 ± 1 Å length, 96 ± 1 Å width), both inhibitor-bound structures possess a longer and more ellipsoid overall shape (122 ± 1 Å length, 92 ± 1 Å width). Superimposition of the two crystallized hexamer conformations shows these differences as a large discrepancy in the RMSD value (Supporting Information Table S11). Individually the conformational change is visible by the rotational twist of the ACT domain relative to the catalytic core by approximately 30° [Fig. 8(C)]. This change is driven by the binding of His at the interface of neighboring domain IIIs, which pulls the complex closer together, significantly increasing the buried surface area of the trimer interface from 830 ± 20 Å^2 (**4YB7**) to 1220 ± 30 Å^2 (**4YB5**/**4YB6**). Very similar changes between the apo and His-bound conformation have also been reported for *Mtu*ATP-PRT, although these changes were not attributed to activity loss.

His binding in both structures occurs at the interface between two adjacent domains III in their trimeric arrangement, similar to the His-bound *Mtu*ATP-PRT structure.[15] Consequently one His is bound per chain, but each chain provides two different faces for the interaction with His. The His carboxyl and amino groups are coordinated via hydrogen bonding interactions with the backbone and Thr252 side chain of the highly conserved binding loop between α9 and β13 of one ACT domain (consensus sequence: PGXXXPT, *Cje*ATP-PRT residues Pro246-Thr252; Supporting Information Fig. S8), whereas the imidazole side chain is inserted into a small cavity created by the side chains on the β-sheet of the other ACT domain, involving interactions with His232', Ser288', Leu290', and a conserved water molecule [Fig. 7(C)].

Comparison to the unoccupied allosteric site in the ATP-bound structure revealed clear differences in the distance and orientation of the two faces of the binding site relative to each other. Although the conserved binding loop does not change its conformation, it is significantly displaced from the adjacent monomer's binding face, with an average distance of 12 Å when His is absent compared to 10 Å when His is bound. Moreover in the presence of His a tight hydrogen bonding network is formed between all three neighboring ACT domains via the residues Thr252, Tyr228, and His266, the conserved water and the bound His molecules, strengthening the interface.

Whereas His binding directly and prominently affects the trimer interface, the catalytic domains also contribute to the overall changes in the hexamer. A large conformational change is not observable (1.02 ± 0.05 Å RMSD between residues 4–225 of the AMP and His-bound and ATP-bound *Cje*ATP-PRT), but changes in the dimer interface are evident comparing the His-bound and ATP-bound structures. The two chains of a dimeric unit undergo a rotational flex [Fig. 8(D)], which elongates the structure (122 ± 1 Å vs. 117 ± 1 Å). The majority of the central dimer interface contacts, involving residues Thr152-Leu163 (α6 and flanking loops) of the first chain and Gln37'-Ile40' (α1-β2 loop), Arg8' (β1), and Asp57' (α2) of the second chain, remain intact upon His binding, but close contacts between residues Thr176-Asn180 (α7) and Gln37'-Ile40' (α1-β2 loop) are lost as the α7 helices are shifted towards the outside of the hexamer. Additional interactions are formed on the opposite side of the dimer interface, as Asn148-Leu151 (β8) and Asp57'-Asp64' (α2) and the C-terminal ends of the α3 helices (Leu87 and Leu87') are now in close proximity to each other. This movement increases the distance between the two active sites by approximately 3 Å (as measured between Lys13 and Ser154) and thereby alters the geometry of the dual-active site cavity.

Although the changes in hexamer conformation are only observed when His is present and are independent from AMP binding to the active site, as seen for of *Eco*ATP-PRT (PDB ID: 1H3D),[11] the AMP and His-bound structure highlights an important inter-subunit contact only occurring at the active site of the inhibited *Cje*ATP-PRT hexamer: The α1-β2 loop (residues Gly29-Pro47), which is involved in the dimer interface formation in the active hexamer, is released upon His binding and protrudes into the active side of a neighboring chain, which brings the side chains of His33' and His35' in close proximity to the PRPP binding loop allowing for additional interactions with the bound inhibitor [Fig. 7(B)] thereby altering the active site further in the presence of His.

Discussion

ATP-PRT acts as the gateway into His biosynthesis and as such plays an important metabolic role. It has been the focus of several studies and identified as a potential target of new antibiotic therapies.[26,27] The nature of the active species in solution of the long form of this enzyme and the details of allostery have been unclear; with early solution studies

favoring a change in quaternary structure from active dimer to inactive His-bound oligomer.[21,22] The loose hexameric structure observed in the absence of His for the *Mtu*ATP-PRT and *Eco*ATP-PRT was interpreted as consistent with an inactive hexamer.[2,11,15] Our solution and crystal studies with *Cje*ATP-PRT support an active homohexamer and illuminate the conformational constriction of this form of the protein as the mechanism for the delivery of allosteric control at the gateway to His biosynthesis.

*Cje*ATP-PRT shares many biochemical and structural properties with the long form ATP-PRT enzymes that have been studied from other sources.[8,10,11,15,19,28] However, extensive kinetic studies are rare. The kinetic parameters determined for *Cje*ATP-PRT are closest to the data reported for *Sen*-ATP-PRT,[8,10] which shares 65% sequence identity with *Cje*ATP-PRT (Supporting Information Fig. S8). Competitive behavior of AMP towards both substrates has been observed for *Cje*ATP-PRT and this has also been shown for the *Sen*ATP-PRT[8] and *Mtu*ATP-PRT[14] enzymes, and it is consistent with the active site binding of AMP where it is observed to be present in both ATP and PRPP binding sites. Direct binding studies using calorimetry, used for the first time here on the *Cje*ATP-PRT protein, are entirely consistent with this interpretation and the competitive inhibition shown by AMP.

Highly complex His binding was observed by calorimetry, consistent with communication and cooperativity between the binding sites. It appears possible that the initial strong exothermic event is based on the rearrangement of the enzyme complex upon His binding, adopting the inhibited state with close contacts at the ACT domain interfaces. It is notable that this strong exothermic signal was not observed when the protein had AMP bound, and that the binding of His becomes less complex when AMP is bound. This result suggests that the constraints on conformation imposed by the AMP facilitate His binding, providing the synergistic response observed in the kinetic measurements both with *Cje*ATP-PRT and with other long form enzymes.[10] A structural rationale for the synergism can be found in the α1-β2 loop, which aids in AMP binding at the neighboring active site in the His-bound hexamer conformation, providing a visible link between active and allosteric binding sites.

We employed SEC and AUC techniques at low concentration of protein to assess the quaternary structure of the enzyme. Our studies provide no evidence for a dimer, even at low concentrations, close to those employed in the kinetic assays. This observation also ruled out quaternary structure change leading to the unusual complex thermogram observed for His binding. A hexameric structure as the active form of *Mtu*ATP-PRT has also been supported in more recent solution experiments.[14]

Our three structures of the hexameric *Cje*ATP-PRT provide insight into key active site interactions and display the changes that are associated with His binding. The clear observation of ATP for the first time in the active site provides a model for the active hexameric form of this enzyme. The binding site of PRPP can be clearly inferred from this structure and from the positioning of AMP in the active site in the AMP/His-bound structure. The reported binding mode for ATP highlights the importance of Mg^{2+} for the ATP-PRT reaction, which was observed to aid in the substrate binding via a double aspartate motif (Asp55-Asp56). Although clearly functional, this metal-binding site along with most other identified binding interactions of ATP is surprisingly not conserved, which stands in stark contrast to the highly conserved PRPP binding motif. Despite the size of the molecule, it therefore seems sufficient for enzymatic efficiency to orientate ATP correctly in the active site, leaving some evolutionary flexibility as to how the binding of its functional groups is achieved in detail.

In the ATP-PRT hexamer all active sites are positioned inside the oligomer, which poses the question how the large, charged substrate and product molecules can enter or leave, if this is the active form of the protein? The hexameric structures of all structurally characterized ATP-PRT long form enzymes possess the same large openings between neighboring domains, which would likely permit access to the interior of the complex. Another possible entrance for substrate molecules is present in form of a small opening in the dimer interface, observed in the ATP-bound structure, which leads directly to the active site and thus may function as a substrate channel. In addition, the dynamic motion of the hexamer may loosen and widen the protein or provide a "breathing" motion, allowing substrate access through the weak interfaces between the catalytic dimer core structure (domains I and II). Some limited evidence for such free movement comes from the thermal stability experiments performed on *Cje*ATP-PRT, which shows a significantly increased (5°C) melting temperature for the inhibitor-bound enzyme. It should also be noted that all chains observed in the hexameric structures of *Cje*ATP-PRT differ marginally from each other, but more so in the ATP-bound crystal resulting in the loss of symmetry.

So what differences in the hexameric form contribute to the low activity of the His-bound form of this protein? As noted above the thermal shift observed is consistent with a rigidification of the structure. His binding to the interfaces of the regulatory trimers found at either end of the core clearly constricts movement of this part of the protein, and

these regulatory trimers are observed to rotate relative to the catalytic hexameric core, which stretches and flexes in turn. The large active site of this protein spans from the hinge between domains I and II to the residues of the dimer interface, and both absolute conformation and conformational flexibility at these areas of the protein are clearly likely to impact on catalysis. Thus in addition to the reduced access to the active site in this closed form of the protein, it seems likely that the conformational restrictions impact directly on catalysis.

Many of the observed conformational and interface changes between His-bound and non His-bound *Cje*ATP-PRT hexamer are also strikingly similar in the reported structures of *Mtu*ATP-PRT and *Eco*ATP-PRT.[11,15] This suggests a common allosteric mechanism for all long form ATP-PRT enzymes. In light of our own work and recent studies on *Mtu*ATP-PRT,[14] this mechanism does not appear to involve the participation of an active dimeric species and must therefore be mediated by the observed changes of the homohexameric molecule. Thus our preferred model of His inhibition to be almost entirely driven by the rotational movement of the domain III. This "twisting of the regulatory tail" alters the overall conformation of the enzyme hexamer impacting on the catalytic properties of the ATP-PRT hexamer.

MATERIAL AND METHODS

Cloning and expression of Cje hisG

The *hisG* gene (locus tag Cj1597) was amplified from *C. jejuni* subsp. *jejuni* NCTC 11168 genomic DNA in three successive nested PCR steps (Supporting Information Table S1), which incorporated a N-terminal tobacco edge virus (TEV) protease cleavage site and the *attB* sites required for subsequent cloning using the Invitrogen Gateway® system. The sequence verified *Cje hisG* was shuttled into expression vector pDEST^{TM}17 and this construct was transformed into expression strain *E. coli* BL21* (DE3) pBB542 + pBB540 (Chaperone 3).

Growth media (LB-Lennox) containing 100 mg/L ampicillin, 25 mg/L chloramphenicol and 100 mg/L spectinomycin was inoculated with a similar overnight preculture (25 mL per L growth) and left to grow at 37°C and 180 rpm until the logarithmical growth phase was reached. After addition of IPTG to a final concentration of 0.5 m*M* the cells were further cultured at 23°C and 180 rpm over night until harvested.

Purification of CjeATP-PRT

Freshly harvested cells were resuspended in lysis buffer (50 m*M* phosphate, 500 m*M* NaCl, 5 m*M* $MgCl_2$, 10 m*M* imidazole, pH 8.0) and lysed by sonication. The clarified supernatant was loaded onto a 5 mL HiTrap^{TM} TALON® crude column (GE Healthcare) and eluted by applying a linear gradient to high-imidazole buffer (50 m*M* phosphate, 500 m*M* NaCl, 5 m*M* $MgCl_2$, 250 m*M* imidazole, pH 8.0) over 35 mL. Protein containing fractions were pooled, mixed with TEV protease in a 1:10 ratio for tag removal. Incubation was performed with an initial 1-h period at 37°C followed by three days at 4°C. The chain retained an N-terminal glycine residue from the protease site. Highly pure *Cje*ATP-PRT was acquired by subsequent size exclusion chromatography using a 26/600 Superdex 200 column (GE Healthcare) with 10 m*M* Tris/HCl, 100 m*M* NaCl, 5 m*M* $MgCl_2$, pH 8.0 as running buffer.

Determination of kinetic parameters

*Cje*ATP-PRT activity was measured *in vitro* using a continuous enzyme assay, based on the work of Ames,[7] directly following the accumulation of the product PR-ATP via the absorbance increase at 290 nm. To force the reaction equilibrium completely onto the product side *E. coli* pyrophosphatase (*Eco* PPase) (Supplementary Material) was added in excess.

The standard reaction mixture contained ATP (2 m*M*), *Cje*ATP-PRT (280 nM), and *Eco*PPase (6.4 μ*M*) in 50 m*M* Tris/HCl, $MgCl_2$ (10 m*M*), NaCl (100 m*M*), KCl (50 m*M*), pH 8.5 at 25°C in a total volume of 1 mL. The reaction was initiated by addition of PRPP (200–300 μ*M*). All assay components were prepared in pre-treated water (Chelex100 resin (BioRad)). ATP and PRPP solutions were mixed in a 1:1 molar ratio with $MgCl_2$.

Kinetic parameters were obtained by fitting the data to the Michaelis-Menten equation using GraFit 5.0 (Erithacus Software) or Prism 6.0 (GraphPad Software). K_M and k_{cat} values were determined using substrate concentrations ranges of 2.5–200 μ*M* for PRPP and 10–2000 μ*M* for ATP. K_i values for His and AMP were obtained from competitive assays against both substrates using concentration ranges of 0.5–3.0 m*M* AMP, 0.01–1.0 m*M* His, 0.08–1.0 m*M* ATP and 0.03–0.3 m*M* PRPP. Excess substrate concentrations were held at 2 m*M* for ATP and 0.3 m*M* for PRPP. Optimal concentrations for Mg^{2+}, Na^+, and K^+ were measured using 0–100 m*M* Mg^{2+}, 0–500 m*M* Na^+, and 0–600 m*M* K^+.

Differential scanning calorimetry

330 μL of degassed 1 mg/mL *Cje*ATP-PRT in 50 m*M* Tris/HCl, 100 m*M* NaCl, 5 m*M* $MgCl_2$, pH 8.5 were analyzed using a NanoDSC (TA Instruments) against the identical buffer. Ligand concentrations used were 2 m*M* AMP and 1 m*M* His. The temperature was increased from 20 to 100°C in increments of 1°C per min under a constant pressure of three atmospheres. Data analysis was performed with the NanoAnalyze software version 3.3.0 (TA Instruments).

Isothermal titration calorimetry (ITC)

ITC experiments were run using a VP-ITC microcalorimeter at 298 K (MicroCal, GE Healthcare). Prior to use all solutions were filtered and degassed under vacuum. All experiments were conducted in 10 m*M* Tris/HCl, 100 m*M* NaCl, 5 m*M* $MgCl_2$, pH 8.5. For K_d measurements ATP (4 m*M*), AMP (3.5 m*M*), and His (1.5 m*M*) were titrated into 100 μ*M* (150 μ*M* in case of ATP) *Cje*ATP-PRT. The synergistic ligand binding effects were investigated using 1 m*M* His (1 m*M* AMP background) and 2 m*M* AMP (1 m*M* His background), respectively. Titrations were performed with 55 injections of ligand: one 2-μL injection followed by fifty-four 5-μL injections. Heat of dilution experiments were measured independently and subtracted from the integrated data before curve-fitting in Origin 7.0.

Analytical ultracentrifugation (AUC)

Sedimentation velocity experiments were performed in a Beckman Coulter model XL-I analytical ultracentrifuge equipped with UV–visible scanning optics. Reference (400 μL of 10 m*M* Tris/HCl, 100 m*M* NaCl, 5 m*M* $MgCl_2$, pH 8.5) and sample (380 μL) solutions were loaded into 12-mm double-sector cells with quartz windows, and the cells were then mounted in an An-50 Ti eight-hole rotor. Proteins were centrifuged at various rotor speeds at 20°C, and radial absorbance data were collected at 230 nm wavelengths, due to the relatively low absorbance of *Cje*ATP-PRT at 280 nm, in continuous mode every 8 min without averaging. Data was fitted to a continuous distribution c(s) model using SEDFIT[29] version 14.6. Partial specific volume (0.7482 g/mL), buffer density (1.00618 cp) and viscosity (0.01033 poise) were calculated using SEDNTERP.[30] The frictional coefficient ratio calculated from the c(s) fit was 1.29.

Protein crystallization and structure determination

After initial screening with a Mosquito® Crystal robot (TTP Labtech) using the PACT *premier*™ HT-96, Clear Strategy™ I HT-96 and Clear Strategy™ II HT-96 screens (Molecular Dimensions), several suitable conditions were identified and further refined. Co-crystallization was achieved in 0.1*M* sodium acetate, 0.1*M* $MgCl_2$, 13–15% w/v PEG 4000, pH 5.5 (ATP), 0.1*M* BTP, 0.2*M* KSCN, 13–14% w/v PEG 3350, pH 6.5 (His) and 0.1*M* Tris, 0.1*M* $MgCl_2$, 13–15% w/v PEG 4000, pH 7.5 (His/AMP). The required *Cje*ATP-PRT concentration was 2.0–3.5 mg/mL and ligand concentrations used were 10 m*M*, 5 m*M* and 1 m*M* for ATP, AMP and His, respectively. All crystals were grown using the hanging drop vapor diffusion method in 24-well VDX plates (Hampton Research). Protein solutions were mixed 1:1 (v/v) with the reservoir solution. The drop size was 2 or 4 μL and the reservoir solution volume 500 μL. Typically crystals were fully formed after 1–3 days. Crystals were cryoprotected in a mix of 20% PEG400 and 80% reservoir solution (His co-crystals) or with 40% glycerol added directly to the drop before looping. Crystals were flash cooled in liquid nitrogen and stored in pucks.

Diffraction data was acquired at the MX1[31] and MX2 beamlines of the Australian Synchrotron. The data was processed using XDS[32] and scaled using the program AIMLESS. Initial phases were solved by a molecular replacement strategy using the CCP4 program suite.[33] The initial search model was generated from *E. coli* ATP-PRT (PDB ID: **1H3D**), containing only domain I and II. A suitable dimeric unit was identified and used in subsequent runs until a hexameric arrangement was found. The missing regulatory domains were added through multiple rounds of refinement using REFMAC5[34] and model building using Coot.[35] The ATP-bound (PDB ID: **4YB7**) and His-bound (PDB ID: **4YB5**) crystal structures were solved following this strategy, while the AMP and His-bound structure (PDB ID: **4YB6**) was solved using the His-bound *Cje*ATP-PRT structure. The structures were validated using the MolProbity server[36] and wwPDB validation server[37] before deposition. All RMSD values given are based on Cα atoms.

Electronic supplementary material: Methods for preparation of *E. coli* pyrophosphatase, mass spectrometry, differential scanning fluorimetry, and results showing metal ion concentration optimization for assays, full kinetic plots, ITC data for ATP binding in the presence of His, thermal stability, size exclusion chromatography, sequences alignment and analysis of interfaces and RMSD values.

Acknowledgments

X-ray data were collected at the MX beamlines of the Australian Synchrotron with access provided by the New Zealand Synchrotron Group.

References

1. Brenner M, Ames BN (1971) *The histidine operon and its regulation*. Metabolic Pathways (Vogel HJ, Ed), 5. Metabolic Regulation, Academic Press Inc., New York.
2. Lohkamp B, Coggins JR, Lapthorn AJ (2000) Purification, crystallization and preliminary X-ray crystallographic analysis of ATP-phosphoribosyltransferase from *Escherichia coli*. Acta Cryst D 56:1488–1491.
3. Sissler M, Delorme C, Bond J, Ehrlich SD, Renault P, Francklyn CS (1999) An aminoacyl-tRNA synthetase paralog with a catalytic role in histidine biosynthesis. Proc Natl Acad Sci USA 96:8985–8990.
4. Vega MC, Zou P, Fernandez FJ, Murphy GE, Sterner R, Popov A, Wilmanns M (2005) Regulation of the hetero-octameric ATP phosphoribosyl transferase complex from *Thermotoga maritima* by a tRNA synthetase-like subunit. Mol Microbiol 55:675–686.

5. Aklujkar M (2011) Two ATP phosphoribosyltransferase isozymes of *Geobacter sulfurreducens* contribute to growth in the presence or absence of histidine and under nitrogen fixation conditions. Can J Microbiol 57:547–558.
6. Francklyn C (2003) tRNA synthetase paralogs: evolutionary links in the transition from tRNA-dependent amino acid biosynthesis to de novo biosynthesis. Proc Natl Acad Sci USA 100:9650–9652.
7. Ames BN, Martin RG, Garry BJ (1961) The first step of histidine biosynthesis. J Biol Chem 236:2019–2026.
8. Morton DP, Parsons SM (1976) Biosynthetic direction substrate kinetics and product inhibition studies on the first enzyme of histidine biosynthesis, adenosine triphosphate phosphoribosyltransferase. Arch Biochem Biophys 175:677–686.
9. Kleemann JE, Parsons SM (1976) Reverse direction substrate kinetics and inhibition studies on the first enzyme of histidine biosynthesis, adenosine triphosphate phosphoribosyltransferase. Arch Biochem Biophys 175:687–693.
10. Morton DP, Parsons SM (1977) Inhibition of ATP phosphoribosyltransferase by AMP and ADP in the absence and presence of istidine. Arch Biochem Biophys 181: 643–648.
11. Lohkamp B, McDermott G, Campbell SA, Coggins JR, Lapthorn AJ (2004) The structure of Escherichia coli ATP-phosphoribosyltransferase: Identification of substrate binding sites and mode of AMP inhibition. J Mol Biol 336:131–144.
12. Winkler ME (1987) *Biosynthesis of histidine. In Escherichia coli and Salmonella typhimurium*. Cell Mol Biol (Neidhardt FC, Ed), 1, American Society for Microbiology, Washington, DC.
13. Martin RG (1963) The first enzyme in histidine biosynthesis: The nature of feedback inhibition by histidine. J Biol Chem 238:257–268.
14. Pedreno S, Pisco JP, Larrouy-Maumus G, Kelly G, de Carvalho LP (2012) Mechanism of feedback allosteric inhibition of ATP phosphoribosyltransferase. Biochemistry 51:8027–8038.
15. Cho Y, Sharma V, Sacchettini JC (2003) Crystal structure of ATP phosphoribosyltransferase from *Mycobacterium tuberculosis*. J Biol Chem 278:8333–8339.
16. Champagne KS, Sissler M, Larrabee Y, Doublie S, Francklyn CS (2005) Activation of the hetero-octameric ATP phosphoribosyl transferase through subunit interface rearrangement by a tRNA synthetase paralog. J Biol Chem 280:34096–34104.
17. Grant GA (2006) The ACT domain: a small molecule binding domain and its role as a common regulatory element. J Biol Chem 281:33825–33829.
18. Lang EJ, Cross PJ, Mittelstädt G, Jameson GB, Parker EJ (2014) Allosteric ACTion: the varied ACT domains regulating enzymes of amino-acid metabolism. Curr Opin Struct Biol 29:102–111.
19. Zhang Y, Shang X, Deng A, Chai X, Lai S, Zhang G, Wen T (2012) Genetic and biochemical characterization of *Corynebacterium glutamicum* ATP phosphoribosyltransferase and its three mutants resistant to feedback inhibition by histidine. Biochimie 94:829–838.
20. Champagne KS, Piscitelli E, Francklyn CS (2006) Substrate recognition by the hetero-octameric atp phosphoribosyltransferase from *Lactocoocus lactis*. Biochemistry 45:14933–14943.
21. Klungsöyr L, Kryvi H (1971) Sedimentation behaviour of phosphoribosyladenosine triphosphate synthase effects of substrates and modifiers. Biochim Biophys Acta 227:327–336.
22. Tebar AR, Fernández VM, MartinDelRio R, Ballesteros AO (1973) Studies on the quaternary structure of the first enzyme of histidine biosynthesis. Experimentia 29:1477–1479.
23. Rao ST, Rossmann MG (1973) Comparison of supersecondary structures in proteins. J Mol Biol 76:241–256.
24. Krissinel E, Henrick K (2007) Inference of macromolecular assemblies from crystalline state. J Mol Biol 372: 774–797.
25. Sinha SC, Smith JL (2001) The PRT protein family. Curr Opin Struct Biol 11:733–739.
26. Cho Y, Ioerger TR, Sacchettini JC (2008) Discovery of novel nitrobenzothiazole inhibitors for *Mycobacterium tuberculosis* ATP phosphoribosyl transferase (HisG) through virtual screening. J Med Chem 51:5984–5992.
27. Lunardi J, Nunes JES, Bizarro CV, Basso LA, Santos DS, Machado P (2013) Targetting the histidine pathway in *Mycobacterium tuberculosis*. Curr Top Med Chem 13:2866–2884.
28. Ohta D, Fujimori K, Mizutani M, Nakayama Y, Kunpaisal-Hashimoto R, Münzer S, Kozaki A (2000) Molecular cloning and characterisation of atp-phosphorybosyl transferase from arabidopsis, a key enzyme in the histidine biosynthetic pathway. Plant Physiol 122:907–914.
29. Schuck P (2000) Size-distribution analysis of macromolecules by sedimentation velocity ultracentrifugation and lamm equation modeling. Biophys J 78:1606–1619.
30. Laue TM, Shah BD, Ridgeway TM, Pelletier SL (1992) *Computeraided interpretation of analytical sedimentation data for proteins*. Analytical Ultracentrifugation in Biochemistry and Polymer Science (al., S. E. H. e., Ed.), Royal Society of Chemistry, Cambridge, United Kingdom.
31. Cowieson NP, Aragao D, Clift M, Ericsson DJ, Gee C, Harrop SJ, Mudie N, Panjikar S, Price JR, Riboldi-Tunnicliffe A, Williamson R, Caradoc-Davies T (2015) MX1: a bending-magnet crystallography beamline serving both chemical and macromolecular crystallography communities at the Australian Synchrotron. J Synchrotron Rad 22:187–190.
32. Kabsch W (2010) XDS. Acta Cryst D 66:125–132.
33. Winn MD, Ballard CC, Cowtan KD, Dodson EJ, Emsley P, Evans PR, Keegan RM, Krissinel EB, Leslie AG, McCoy A, McNicholas SJ, Murshudov GN, Pannu NS, Potterton EA, Powell HR, Read RJ, Vagin A, Wilson KS (2011) Overview of the CCP4 suite and current developments. Acta Cryst D 67:235–242.
34. Murshudov GN, Vagin A, Dodson EJ (1997) Refinement of macromolecular structures by the maximum-likelihood method. Acta Cryst D 53:240–255.
35. Emsley P, Lohkamp B, Scott W, Cowtan KD (2010) Features and development of coot. Acta Cryst D 66: 486–501.
36. Chen VB, Arendall WB, Headd JJ, Keedy DA, Immormino RM, Kapral GJ, Murray LW, Richardson JS, Richardson DC (2010) MolProbity: all-atom structure validation for macromolecular crystallography. Acta Cryst D 66:12–21.
37. Read RJ, Adams PD, Arendall WB, 3rd Brunger AT, Emsley P, Joosten RP, Kleywegt GJ, Krissinel EB, Lutteke T, Otwinowski Z, Perrakis A, Richardson JS, Sheffler WH, Smith JL, Tickle IJ, Vriend G Zwart PH (2011) A new generation of crystallographic validation tools for the protein data bank. Structure 19:1395–1412.